


Dispersion control in coupled channel-heterogeneous porous media systems

Bowen Ling 

*Institute of Mechanics, Chinese Academy of Sciences, Beijing 100190, China
and School of Engineering Science, University of Chinese Academy of Sciences, Beijing 100049, China*

Runqing Shan

School of Engineering Science, University of Chinese Academy of Sciences, Beijing 100049, China

Felipe P. J. de Barros 

Sonny Astani Department of Civil and Environmental Engineering, University of Southern California, Los Angeles, California 90089, USA



(Received 29 January 2024; accepted 21 May 2024; published 17 June 2024)

Multilayered porous media can be found widely in both natural and engineered systems. This type of heterogeneous porous structure can have a substantial influence on the effective flow and transport processes. This work aims to develop a hybrid analytical-numerical solution that elucidates the relationship between the scalar dynamics and media properties in a coupled system comprising a two-dimensional free-flow layer and a heterogeneous porous medium, operating under fully developed laminar flow conditions. In our study, we employ perturbation and homogenization methods to derive a set of one-dimensional upscaled equations for transport of a passive scalar. Subsequently, we develop an integral transform-based semianalytical solution that allows to relate the properties of the porous system to scalar mixing and spreading. To validate the newly developed solution for the upscaled system, we compare it with the numerical results for the two-dimensional scalar transport. The semianalytical solution is used to investigate the influence of the multilayered system on macroscopic transport by analyzing the scalar cloud's breakthrough curve, dispersion coefficient, and mixing. Our findings indicate that the semianalytical solution can be utilized to optimize and control dispersion of the scalar cloud. Our computational results show the potential of the solution to determine the arrangement of porous media properties to achieve a desired mixing objective.

DOI: [10.1103/PhysRevFluids.9.064502](https://doi.org/10.1103/PhysRevFluids.9.064502)

I. INTRODUCTION

Scalar transport in conduits embedded in a porous permeable matrix is ubiquitous in both natural and engineered systems. Examples consist of fractured porous media [1], canopy-coated riverbeds [2], porous-wall microfluid mixers [3], blood vessels [4,5], membrane filters and microthermophotovoltaic generators [6,7], and altered zones induced by geochemical reactions in geological systems [8–10]. The presence of shear due to the interaction of the free flow with a porous surface can regulate and control momentum and mass fluxes between adjacent systems [11–14]. Channels that are coated with multiple layers of porous media exhibit distinct properties that impact the flow and migration of solutes at both micro and macro scale. In our study, the microscale refers to the specific physical domain where pore morphology and concentration are defined at individual points, whereas the macroscale encompasses the overall media and transport characteristics represented by effective properties such as dispersion. The arrangement of these layers, as well as any structural variations within a single layer, can influence the overall transport capabilities (e.g., dispersion) of the system.

Therefore, establishing a fundamental understanding of the relationship between the microstructure and transport properties is essential for precise prediction of scalar mass migration, optimization of microdispersion, and other related tasks.

Three modeling strategies are commonly employed when investigating scalar dispersion in a coupled channel-matrix system. These are:

(1) *Direct numerical method.* This approach utilizes numerical simulations to accurately predict solute migration within the system. It consists of solving the multidimensional advection-diffusion equations in both the porous layers and the free-flow domains. While it provides high-fidelity results, the computationally intensive nature of the direct numerical approach limits its widespread application due to the inherent multiscale nature of the channel-matrix system. Discrete fracture network (DFN) models [15,16] are frequently applied for complex fracture networks to reduce the computational burden of the direct numerical method.

(2) *Analytical solutions of advection-diffusion equations.* These solutions involve quantifying the transport by means of the ADE. However, obtaining analytical solutions is often feasible only under simplifying assumptions. One of the major technical difficulties lies in accounting for the non-uniformity of the velocity profile in the channel and/or matrix [17–19]. As a result, the analytical analysis often assumes uniform velocity, pure diffusive transport, or de-coupled channel-matrix transport. Hybrid analytical-numerical methods, such as the one adopted in de Barros and Cotta [20], allow for more flexibility in considering the variability of both the velocity and diffusivity profiles directly in the ADE.

(3) *Upscaling methods.* Upscaling methods involve the estimation of effective parameters by averaging over heterogeneous domains or by modeling the system using simplified representations. These approaches aim to capture the overall dispersive behavior of the scalar cloud in the coupled channel-matrix system while reducing computational complexity. Often times, analytical solutions can be employed to solve the simplified representation of the governing equations due to the complexity reduction.

Within the context of hydrological applications and waste disposal safety assessment, Tang *et al.* [21] and Sudicky and Frind [1] proposed the use of analytical solutions to predict reactive contaminant transport in fractured porous media. The works of Tang *et al.* [21] and Sudicky and Frind [1] assume that transverse diffusion is the sole physical mechanism for solute migration within the porous matrix and that transport in the fracture is due to longitudinal advection and dispersion. Along this line of work, Roubinet *et al.* [17] expanded previous solutions (e.g., Refs. [1,21]) to examine solute transport in a single fracture embedded in a porous medium. Roubinet *et al.* [17] showed, semianalytically, how transverse dispersion within a fracture controlled fracture-matrix solute exchange. In similar fashion, Dejam *et al.* [22] derived a solution for an upscaled transport model of a fracture-porous matrix system and highlighted the importance of fracture-matrix interaction in controlling the magnitude of the dispersion coefficient. Rubol *et al.* [23] proposed a hybrid numerical-analytical methodology to examine the impact of the velocity profile in a turbulent shear flow over a permeable canopy layer on scalar mass fluxes in a two-dimensional system. The authors illustrated how the permeability and porosity of the permeable layer affected the asymmetry of the scalar concentration spatial profile [23]. Due to its flexibility to tackle more complex scenarios, these hybrid numerical-analytical methods have also been employed to continuum and discrete flow and transport models for fractured porous media [13,24]. The derivation of analytical solutions for the scalar concentration field has also been subject of interest in other applications, such as microfluidic devices and biological fluids. Dejam [12] derived a reduced order model to examine the effects of both pressure-driven and electroosmotic flows on hydrodynamic dispersion in a porous-walled microfluidic channel. Motivated by the cardiovascular system, Zimmerman *et al.* [25] used Laplace's transform to derive analytical solutions for an upscaled reactive advection-dispersion equation in a tube with diffusive losses through the tube's walls.

To attain closed-form solutions, some of the above-mentioned works relied on upscaling techniques to reduce the complexity of the transport process in the channel-porous matrix system. The upscaling method involves various perturbation techniques, such as single- or multiple-scale

expansions and Reynolds-type decomposition. These methods allow for a rigorous derivation of macroscale equations that describe the spatially averaged quantities at the microscale (pore-scale). Examples of such techniques include homogenization [26], volume averaging [27], and the method of moments [28]. These approaches establish a formal connection between the micro- and macroscale by introducing effective parameters, such as the dispersion coefficients, which depend on the specific characteristics of the coupled channel-matrix system. These upscaling methods provide asymptotic approximations of the complete microscopic solution, typically truncated at the first or second order.

Despite significant insights obtained in the above mentioned literature, most of these works assume that the porous matrix is homogeneous (for an exception, see Ref. [24]). Multilayer porous media possesses distinctive characteristics and benefits that make it indispensable across a wide range of applications in natural and engineered systems. Examples of such composite porous media include stratified soils [29,30], landfill clay liners [31], and multilayered membrane filters [7]. Natural systems, such as shales and aquifers, are typically characterized by multiple layers of media that display distinctive transport properties and demonstrate a multiscale nature (e.g., Refs. [29,30,32]). Such stratification in the geological properties, e.g., permeability, can lead to non-Fickian transport behavior [29,33,34]. As an example from engineered systems, a multilayered porous membrane consists of multiple stacked membranes, each serving a distinct purpose. Some layers provide structural support, while others function as filters for substances of varying sizes. The resulting layered system exhibits exceptional flow and transport properties, notably including permeability and dispersion. Sanaei and Cummings [6] developed a physics-based model for these multilayered systems that allows to investigate the influence of the membrane's morphological features in the filtration performance. The model proposed in Sanaei and Cummings [6] is also used to optimize the membrane's structure to achieve a desired goal. Experimental evidence has shown that a meticulously engineered multilayer membrane outperforms a uniform membrane [35].

The main goal of our analysis is to examine transport of a passive scalar through a symmetric free-flow layer (FFL) embedded within a multilayered porous media (PML) system. The PML is characterized by its spatially variable permeability and porosity. Our objective is to establish an analytical relationship between the macroscopic behavior of the coupled FFL-PML system, specifically the breakthrough condition, dispersion, and mixing, with the properties that characterise the multilayered media. To achieve this, we combine spatial averaging with perturbation approaches to explicitly consider both the impact of steady non-uniform flow conditions and a multilayer porous matrix on dispersion of the scalar cloud. The upscaled concentration field is computed by means of integral transforms. For the purpose of illustration, we assume the flow in the FFL is governed by the Stokes equation, while the flow within the PML is described by Darcy-Brinkman's equation (e.g., Refs. [36,37]). The solution methodology for the scalar problem can account for other flow models within the PML. Our results highlight how the hydraulic properties characterizing the multilayer porous medium have the potential of modulating the dispersive behavior of a solute.

II. PHYSICAL MODEL AND ASSUMPTIONS

A. Velocity profile in multilayer system

The domain of interest (Fig. 1) is composed of multiple layers, including one FFL and several PMLs. In this study, tilde ($\tilde{\cdot}$) denotes dimensional variables. The FFL occupies $\tilde{x} \in (0, L)$ and $\tilde{y} \in (0, H_0)$, and the n th PML occupies $\tilde{x} \in (0, L)$ and $\tilde{y} \in (\mathbb{H}_0^{n-1}, \mathbb{H}_0^n)$, where L is the length of the domain and \mathbb{H}_a^b represents a summation operation:

$$\mathbb{H}_a^b = \sum_{i=a}^b H_i, \quad (1)$$

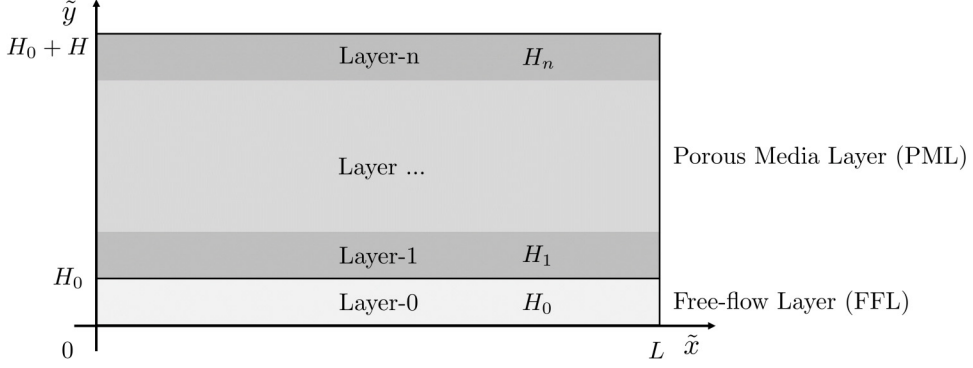


FIG. 1. Schematic representation of the two-dimensional flow domain. Layer-0 represent the free-flow layer. The remaining layers (Layer-1, Layer-2,...,Layer- n) represents porous materials characterized by distinct permeabilities.

and H_i , $i = 0, 1, 2, \dots, n$ is the width of the i th layer. Namely, the width of the FFL is H_0 and the total width of the PML is defined as

$$H = \mathbb{H}_1^n. \quad (2)$$

The fluid flow in the FFL is incompressible and modelled with Stokes' equation:

$$\mu \frac{d^2 \tilde{u}_0}{d\tilde{y}^2} - \frac{d\tilde{p}}{d\tilde{x}} = 0, \quad \text{for } \tilde{y} \in [0, H_0], \quad (3)$$

where μ is the viscosity, \tilde{u}_0 is the longitudinal velocity in the FFL (Layer-0 in Fig. 1), and $d\tilde{p}/d\tilde{x}$ is the pressure gradient along \tilde{x} . The pressure gradient is defined by

$$\frac{d\tilde{p}}{d\tilde{x}} = \frac{P_L - P_0}{L}, \quad (4)$$

where P_0 and P_L are the pressures at the inlet and outlet respectively. We define the outlet pressure $P_L = 0$, hence the pressure gradient becomes $-P_0/L$.

The flow in the PML is assumed to be governed by the Darcy-Brinkman equation:

$$\mu \frac{d^2 \tilde{u}_i}{d\tilde{y}^2} - \frac{\mu}{K_i} \tilde{u}_i - \frac{d\tilde{p}}{d\tilde{x}} = 0, \quad \text{for } \tilde{y} \in [\mathbb{H}_0^{i-1}, \mathbb{H}_0^i], \quad (5)$$

with K_i and \tilde{u}_i denoting the permeability and velocity in the i th porous layer. Here \tilde{u}_i is non-zero only in the i th porous layer. In this model, the flow is parallel to the PML, and is symmetric about $\tilde{y} = 0$. Notice that other models, besides the Darcy-Brinkman equation, could be adopted in this work. The Darcy-Brinkman model is employed here for the purpose of illustration. Noticeably, velocity profiles of the FFL and PML are assumed to be fully developed along the longitudinal direction. In this work, the following boundary conditions are adopted:

$$\frac{d\tilde{u}_0}{d\tilde{y}} = 0, \quad \tilde{y} = 0, \quad (6)$$

$$\tilde{u}_i = \tilde{u}_{i+1}, \quad \tilde{y} = \mathbb{H}_0^i, \quad i = \{0, 1, 2, \dots, n-1\}, \quad (7)$$

$$\frac{d\tilde{u}_i}{d\tilde{y}} = \frac{d\tilde{u}_{i+1}}{d\tilde{y}}, \quad \tilde{y} = \mathbb{H}_0^i, \quad i = \{0, 1, 2, \dots, n-1\}, \quad (8)$$

$$\tilde{u}_n = 0, \quad \tilde{y} = \mathbb{H}_0^n. \quad (9)$$

The velocity of the FFL and PML are:

$$\tilde{u}_f = \tilde{u}_0, \quad (10)$$

$$\tilde{u}_m = \sum_i \tilde{u}_i. \quad (11)$$

We normalize the governing flow equations according to the following groups:

$$u_i = \frac{\tilde{u}_i}{U_0}, \quad x = \frac{\tilde{x}}{L}, \quad y = \frac{\tilde{y}}{H_0}, \quad (12)$$

where U_0 is the characteristic velocity. Equations (3) and (5) then become

$$\frac{d^2 u_0}{dy^2} + \frac{H_0^2 P_0}{\mu L U_0} = 0, \quad \text{for } y \in [0, 1], \quad (13)$$

and

$$\mu \frac{d^2 u_i}{dy^2} - \frac{H_0^2}{K_i} u_i + \frac{H_0^2 P_0}{\mu L U_0} = 0, \quad \text{for } y \in [h^{i-1}, h^i], \quad (14)$$

where $h^i = \mathbb{H}_0^i$ and $h_0 = H_0/H_0 = 1$. U_0 is the dimensional velocity scale defined as $U_0 = H_0^2 P_0 / (\mu L)$. Additionally, We define the following dimensionless parameters:

$$\lambda_i = \frac{H_0}{\sqrt{K_i}}, \quad k_i = \frac{1}{\lambda_i} = \frac{\sqrt{K_i}}{H_0}, \quad (15)$$

where λ is the reciprocal of the Darcy number. We have the dimensionless system of equations

$$\frac{d^2 u_0}{dy^2} + 1 = 0, \quad \text{for } y \in [0, 1], \quad (16)$$

$$\frac{d^2 u_i}{dy^2} - \lambda_i^2 u_i + 1 = 0, \quad \text{for } \tilde{y} \in [h^{i-1}, h^i], \quad (17)$$

with the corresponding dimensionless boundary equations

$$\frac{du_0}{dy} = 0, \quad y = 0, \quad (18)$$

$$u_i = u_{i+1}, \quad y = h^i, \quad i = \{0, 1, 2, \dots, n-1\}, \quad (19)$$

$$\frac{du_i}{dy} = \frac{du_{i+1}}{dy}, \quad y = h^i, \quad i = \{0, 1, 2, \dots, n-1\}, \quad (20)$$

$$u_n = 0, \quad y = h^n. \quad (21)$$

The general solution of the ordinary differential equation system given by Eqs. (16) and (17) is

$$u_0(y) = -\frac{1}{2}y^2 + E_0 y + F_0, \quad \text{for } y \in [0, 1], \quad (22)$$

$$u_i(y) = \frac{1}{\lambda_i^2} + E_i e^{\lambda_i y} + F_i e^{-\lambda_i y}, \quad \text{for } \tilde{y} \in [h^{i-1}, h^i], \quad (23)$$

where $E_0, F_0, E_i,$ and F_i are integration constants to be determined by boundary conditions. We have

$$E_0 = 0, \quad (24)$$

$$-\frac{1}{2}h_0^2 + E_0 h_0 F_0 - \frac{1}{\lambda_1^2} - E_1 e^{\lambda_1 h_0} - F_1 e^{-\lambda_1 h_0} = 0, \quad (25)$$

$$-h_0 + E_0 - E_1 \lambda_1 e^{\lambda_1 h_0} + F_1 \lambda_1 e^{-\lambda_1 h_0} = 0, \quad (26)$$

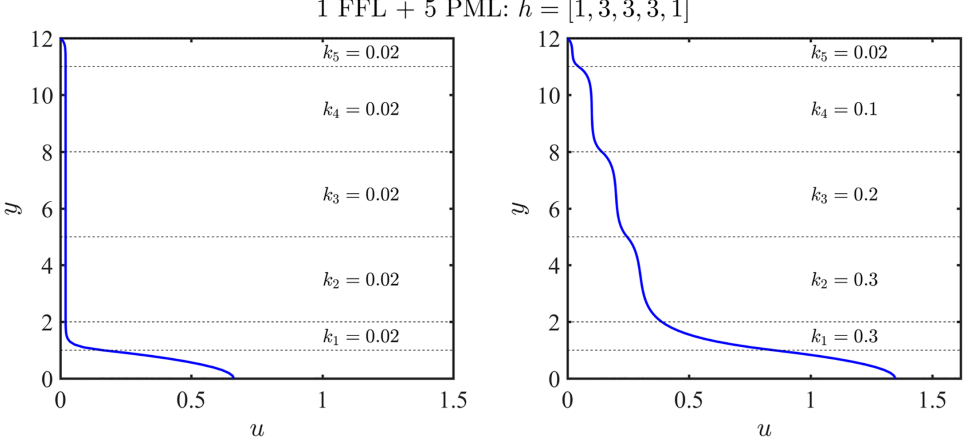


FIG. 2. Left: Velocity profile of a six-layer system where $\{k_i\}_{i=1}^5 = 0.02$. Right: Velocity profile of a six-layer system where $[k_1, k_2, k_3, k_4, k_5] = [0.3, 0.3, 0.2, 0.1, 0.02]$.

$$\frac{1}{\lambda_i^2} + E_i e^{\lambda_i h^{i-1}} + F_i e^{-\lambda_i h^{i-1}} - \frac{1}{\lambda_{i-1}^2} - E_{i-1} e^{\lambda_{i-1} h^{i-1}} - F_{i-1} e^{-\lambda_{i-1} h^{i-1}} = 0, \quad (27)$$

$$E_i \lambda_i e^{\lambda_i h^{i-1}} - F_i \lambda_i e^{-\lambda_i h^{i-1}} - E_{i-1} \lambda_{i-1} e^{\lambda_{i-1} h^{i-1}} + F_{i-1} \lambda_{i-1} e^{-\lambda_{i-1} h^{i-1}} = 0, \quad (28)$$

$$-E_n e^{\lambda_n h^n} - F_n e^{-\lambda_n h^n} - \frac{1}{\lambda_n^2} = 0. \quad (29)$$

Notice that Eqs. (27) and (28) are valid for $i = 2, 3, \dots, n$, and there are $2n + 2$ equations from Eqs. (24)–(29). A system of linear equations can be constructed to solve for the unknowns $[E_0, F_0, \dots, E_i, F_i]$. The final solution will provide the velocity profile within the FFL and PML.

The velocity profile of a six-layer system with two permeability profiles is shown in Fig. 2. The system consists of one FFL layer and five PML layers. Figure 2 (left) corresponds to the case where the permeability values are identical, viz. $[k_1, k_2, k_3, k_4, k_5] = [0.02, 0.02, 0.02, 0.02, 0.02]$, while the Fig. 2 (right) depicts the result of a heterogeneous structure, viz. $[k_1, k_2, k_3, k_4, k_5] = [0.3, 0.3, 0.2, 0.1, 0.02]$. From Fig. 2, we can observe that when the permeabilities are low and uniform, the velocity shear stems from the FFL (Fig. 2, left). However, the velocity profile becomes more fluctuating when the permeability is heterogeneous (Fig. 2, right) with shear flow throughout the entire PML-FFL system. It is worth noting that when upscaling the concentration equation, other velocity profiles can also be considered. For example, the coupling of the Stokes and Darcy equations with the Beavers-Joseph interface condition [38] can be taken into account.

B. Scalar transport and upscaling

We model transport of a passive scalar with a two-dimensional advection-diffusion equation in the FFL and a two-dimensional advection-dispersion equation for the PML. The scalar quantity is instantaneously injected into the FFL. The evolution of the scalar concentration in time and space is given by the following equations:

$$\frac{\partial \tilde{c}_1}{\partial \tilde{t}} + \tilde{u}_f \frac{\partial \tilde{c}_1}{\partial \tilde{x}} = \tilde{D}_1 \frac{\partial^2 \tilde{c}_1}{\partial \tilde{x}^2} + \tilde{D}_1 \frac{\partial^2 \tilde{c}_1}{\partial \tilde{y}^2}, \quad \text{For } \tilde{y} \in [0, H_0], \quad (30)$$

$$\frac{\partial \tilde{c}_2}{\partial \tilde{t}} + \tilde{u}_m \frac{\partial \tilde{c}_2}{\partial \tilde{x}} = \tilde{D}_2 \frac{\partial^2 \tilde{c}_2}{\partial \tilde{x}^2} + \tilde{D}_2 \frac{\partial^2 \tilde{c}_2}{\partial \tilde{y}^2}, \quad \text{For } \tilde{y} \in [H_0, \mathbb{H}_0^n], \quad (31)$$

where $\tilde{c}_1(\tilde{x}, \tilde{t})$ and $\tilde{c}_2(\tilde{x}, \tilde{t})$ are the local scalar concentrations in the FFL and PML, respectively, \tilde{u}_f and \tilde{u}_m are the longitudinal velocities, \tilde{D}_1 is the diffusion coefficient in the FFL, and \tilde{D}_2 is the mechanical dispersion coefficient of the PML (assumed to be isotropic). We define dimensionless variables as follows:

$$c_{1,2}(x, t) = \frac{\tilde{c}_{1,2}}{C_0}, \quad u_{f,m} = \frac{\tilde{u}_{f,m}}{U_0}, \quad D_{1,2} = \frac{\tilde{D}_{1,2}}{D_0}, \quad t = \frac{\tilde{t}}{T}, \quad (32)$$

where D_0 is the scale of diffusion coefficient and T is timescale, in this study, we choose $T = L/U_0$. We utilize consistent scaling for both the FFL and PML layers, ensuring that these scales are distinctive and representative for the entire system. As an example, the concentration and velocity scales are unique for both FFL and PML. Additionally, the diffusivity D_0 corresponds to the molecular diffusion of the solute and serves as a representative value of the entire system. Further we define two dimensionless quantities:

$$\text{Pe} = \frac{H_0 U_0}{D_0}, \quad \epsilon = \frac{H_0}{L}, \quad (33)$$

where Pe is the Péclet number and ϵ is the length ratio of the system (see Fig. 1). The dimensionless transport equations are

$$\text{Pe} \frac{\partial c_1}{\partial t} + \text{Pe} u_f \frac{\partial c_1}{\partial x} = \epsilon^2 D_1 \frac{\partial^2 c_1}{\partial x^2} + D_1 \frac{\partial^2 c_1}{\partial y^2}, \quad \text{for } y \in [0, 1], \quad (34)$$

$$\text{Pe} \frac{\partial c_2}{\partial t} + \text{Pe} u_m \frac{\partial c_2}{\partial x} = \epsilon^2 D_2 \frac{\partial^2 c_2}{\partial x^2} + D_2 \frac{\partial^2 c_2}{\partial y^2}, \quad \text{for } y \in [1, h^n], \quad (35)$$

where u_f is the velocity profile of the FFL (i.e., $u_f = u_0$), and u_m is the velocity of the entire PML (i.e., $u_m = \sum_i u_i$). The corresponding boundary conditions are

$$c_1 = 0, \quad x = 0; \quad \frac{\partial c_1}{\partial x} = 0, \quad x = L, \quad (36)$$

$$\frac{\partial c_2}{\partial x} = 0, \quad x = 0; \quad \frac{\partial c_2}{\partial x} = 0, \quad x = L, \quad (37)$$

$$\frac{\partial c_1}{\partial y} = 0, \quad y = 0; \quad c_1 = c_2, \quad y = 1, \quad (38)$$

$$D_1 \frac{\partial c_1}{\partial y} = \phi D_2 \frac{\partial c_2}{\partial y}, \quad y = 1; \quad \frac{\partial c_2}{\partial y} = 0, \quad y = h^n, \quad (39)$$

$$c_1 = \mathcal{N}(x|\mu_0, \sigma_0), \quad t = 0; \quad c_2 = 0, \quad t = 0, \quad (40)$$

where $\mathcal{N}(x|\mu_0, \sigma_0)$ is the Gaussian probability density function with mean μ_0 and standard deviation σ_0 :

$$\mathcal{N}(x|\mu_0, \sigma_0) = \frac{1}{\sigma_0 \sqrt{2\pi}} e^{-\frac{(x-\mu_0)^2}{2\sigma_0^2}}. \quad (41)$$

Despite our choice for a Gaussian-like instantaneous injection, other functions can be employed *in lieu* of $\mathcal{N}(x|\mu_0, \sigma_0)$. ϕ is the porosity, which is the ratio between the void space and the total volume of the media.

To upscale this system of equations, see Eqs. (34) and (35), we employ a spatial transformation together with homogenization upscaling techniques following the work of Ling *et al.* [3]. Let η denote the spatial transformation

$$\eta = \epsilon^{-\frac{1}{2}} x, \quad (42)$$

and

$$c_1 = c_1^{(0)}(t, \eta) + \epsilon^{\frac{1}{2}} c_1^{(1)}(t, \eta, y) + \epsilon c_1^{(2)}(t, \eta, y) + O[\epsilon^{\frac{3}{2}}], \quad (43)$$

$$c_2 = c_2^{(0)}(t, \eta) + \epsilon^{\frac{1}{2}} c_2^{(1)}(t, \eta, y) + \epsilon c_2^{(2)}(t, \eta, y) + O[\epsilon^{\frac{3}{2}}]. \quad (44)$$

Equations (43) and (44) represent a homogenization expansion of order $\epsilon^{\frac{1}{2}}$. By substituting Eqs. (42)–(44) into Eqs. (34) and (35), we obtain two expanded expressions, namely, Eqs. (A1) and (A2) (see Appendix A). These expanded equations can be rearranged and combined to form a system of equations, specifically Eqs. (A3)–(A5) and (A6)–(A8). By solving these equations sequentially, we can determine $c_1^{(1)}$, $c_1^{(2)}$, $c_2^{(1)}$, and $c_2^{(2)}$. Subsequently, these values are substituted back into the expanded Eqs. (A1) and (A2). Finally, spatial averaging is performed along the y -direction, taking into account the boundary conditions. This process yields the coupled upscaled equations described in Refs. [3,13] (see Appendix A for details):

$$\frac{\partial c_1^{(0)}}{\partial t} + \langle u_f \rangle \frac{\partial c_1^{(0)}}{\partial x} = D_1^* \frac{\partial^2 c_1^{(0)}}{\partial x^2} + A_1 \frac{\partial c_1^{(0)}}{\partial x} + A_2 (c_1^{(0)} - c_2^{(0)}), \quad (45)$$

$$\frac{\partial c_2^{(0)}}{\partial t} + \langle u_m \rangle \frac{\partial c_2^{(0)}}{\partial x} = D_2^* \frac{\partial^2 c_2^{(0)}}{\partial x^2} - B_1 \frac{\partial c_2^{(0)}}{\partial x} - B_2 (c_1^{(0)} - c_2^{(0)}), \quad (46)$$

subject to

$$c_1^{(0)} = 0, \quad x = 0; \quad \frac{\partial c_1^{(0)}}{\partial x} = 0, \quad x = L, \quad (47)$$

$$\frac{\partial c_2^{(0)}}{\partial x} = 0, \quad x = 0; \quad \frac{\partial c_2^{(0)}}{\partial x} = 0, \quad x = L, \quad (48)$$

$$c_1^{(0)} = \mathcal{N}(\mu_0, \sigma_0), \quad t = 0; \quad c_2^{(0)} = 0, \quad t = 0, \quad (49)$$

where $\langle \cdot \rangle$ is the spatial average operator:

$$\langle \cdot \rangle = \frac{1}{L^*} \int_0^{L^*} \cdot \, dy, \quad (50)$$

where $L^* = 1$ for the FFL and $L^* = h^n - 1$ for the PML. The upscaled dispersion coefficients are given by

$$D_1^* = \frac{\epsilon D_1}{\text{Pe}} - \frac{\epsilon \text{Pe}}{D_1} \langle u_f M(y) \rangle, \quad (51)$$

$$D_2^* = \frac{\epsilon D_2}{\text{Pe}} - \frac{\epsilon \text{Pe}}{D_2} \langle u_m N(y) \rangle, \quad (52)$$

and A_1 , A_2 , B_1 , and B_2 are the upscaled coefficients reported in Appendix B. $M(y)$ and $N(y)$ are the characteristic function of dispersivity (see Appendix B). Additionally, in Appendix C, we show that the D_1^* approaches to the classic Taylor-Aris dispersion when the permeability approaches zero.

The higher-order concentration solutions are also solved:

$$c_1^{(1)}(x, y, t) = \frac{\epsilon^{\frac{1}{2}} \text{Pe}}{D_1} M(y) \frac{\partial c_1^{(0)}}{\partial x}, \quad (53)$$

$$c_2^{(1)}(x, y, t) = \frac{\epsilon^{\frac{1}{2}} \text{Pe}}{D_2} N(y) \frac{\partial c_2^{(0)}}{\partial x}, \quad (54)$$

The upscaled Eqs. (45) and (46) are solved for the zeroth-order concentrations, namely, $c_1^{(0)}$ and $c_2^{(0)}$. The first-order concentration profile is calculated according to Eqs. (53) and (54). And these expressions will be used to reconstruct two-dimensional distribution.

III. SOLUTION METHODOLOGY

A. Generalized integral transform technique

To solve the governing transport Eqs. (45) and (46) along with its initial and boundary conditions (47) and (48), we will make use of the *Generalized Integral Transform Technique*, i.e., GITT [39,40]. This method has been applied to compute scalar transport in shear flows [20,23,41]. In flow and scalar transport related study, many governing equations exhibit a similar form as that of Eqs. (45) and (46), thus, to enhance generality, we rewrite the upscaled equations in the following manner:

$$\frac{\partial C_1}{\partial t} = \frac{\partial}{\partial x} \left(P_1 \frac{\partial C_1}{\partial x} \right) + P_2 \frac{\partial C_1}{\partial x} + P_3 \frac{\partial C_2}{\partial x} + P_4 C_1 + P_5 C_2, \quad (55)$$

$$\frac{\partial C_2}{\partial t} = \frac{\partial}{\partial x} \left(Q_1 \frac{\partial C_2}{\partial x} \right) + Q_2 \frac{\partial C_2}{\partial x} + Q_3 \frac{\partial C_1}{\partial x} + Q_4 C_2 + Q_5 C_1, \quad (56)$$

where $C_{1,2} \equiv \langle c_{1,2} \rangle \equiv c_{1,2}^{(0)}$. The connection between Eqs. (45), (46) and (55), (56) is provided through the coefficients P_i and Q_i ($i = 1, 2, \dots, 5$) which are reported in Appendix B. Note that all P_i and Q_i are constants once the geometric and transport parameters of the FFL and PML are determined. The boundary and initial conditions are as follows:

$$C_1(0, t) = 0; \quad \left. \frac{\partial C_1}{\partial x} \right|_{x=L} = 0; \quad C_1(x, 0) = \mathcal{N}(x|\mu_0, \sigma_0), \quad (57)$$

$$C_2(0, t) = 0; \quad \left. \frac{\partial C_2}{\partial x} \right|_{x=L} = 0; \quad C_2(x, 0) = 0, \quad (58)$$

We start by defining the integral transform-inverse pair [39,42]:

$$\bar{C}_{ji}(t) = \int_0^L \tilde{\xi}_{ji}(x) C_j(x, t) dx, \quad j = \{1, 2\}, \quad (59)$$

$$C_j(x, t) = \sum_{i=1}^{\infty} \tilde{\xi}_{ji}(x) \bar{C}_{ji}(t), \quad j = \{1, 2\}, \quad (60)$$

where the symmetric kernels (i.e., eigenfunctions) $\tilde{\xi}_{ji}(x)$ are defined as follows:

$$\tilde{\xi}_{ji}(x) \equiv \frac{\xi_{ji}(x)}{\sqrt{N_{ji}}}, \quad j = \{1, 2\}. \quad (61)$$

Here, N_{ji} corresponds to the norm of the eigenfunctions $\xi_{ji}(x)$. The norm is defined as the integral over the eigenfunction squared over the entire domain [39,42], and it is written as

$$N_{ji} = \int_0^L \xi_{ji}^2(x) dx. \quad (62)$$

The kernels are the solution of the eigenvalue problem:

$$\frac{\partial}{\partial x} \left(P_1 \frac{\partial \xi_{1i}}{\partial x} \right) + P_4 \xi_{1i} = -\mu_{1i}^2 \xi_{1i}, \quad (63)$$

$$\frac{\partial}{\partial x} \left(Q_1 \frac{\partial \xi_{2i}}{\partial x} \right) + Q_4 \xi_{2i} = -\mu_{2i}^2 \xi_{2i}, \quad (64)$$

where μ_{ji} are the eigenvalues, these equations are subject to

$$\xi_{ji}(0) = 0; \quad \left. \frac{\partial \xi_{ji}}{\partial x} \right|_{x=L} = 0. \quad (65)$$

In our upcoming examples, we consider P_i and Q_i (for $i = 1, 2, \dots$) to be constant. A set of solutions for Eqs. (63), given constant P_i and Q_i (for $i = 1, 2, \dots, 5$), satisfying the boundary conditions

defined in Eq. (65) is

$$\xi_{ji}(x) = \sin(\beta_{ji}x), \quad (66)$$

where β_{ji} are the positive roots of $\cos(\beta_{ki}L) = 0$, we write

$$\beta_{ji} = \frac{n\pi}{L} + \frac{2\pi}{L}, \quad n = 0, 1, 2, \dots \quad (67)$$

Multiplying Eqs. (55) and (56) by $\xi_{ji}(x)$, integrating from 0 to L and using Eqs. (59) and (60) together with the boundary conditions, we obtain the following set of coupled ordinary differential equations (for details, see Ref. [39]):

$$\frac{d\bar{C}_{ji}(t)}{dt} + \mu_{ji}^2 \bar{C}_{ji}(t) = \bar{G}_{ji}(\bar{C}_{1i}(t), \bar{C}_{2i}(t)), \quad j = \{1, 2\}, \quad (68)$$

with

$$\mu_{1i} = \sqrt{P_1 \beta_{1i}^2 - P_4}, \quad (69)$$

$$\mu_{2i} = \sqrt{Q_2 \beta_{2i}^2 - Q_4}. \quad (70)$$

The function $\bar{G}_{ji}(\bar{C}_{1i}, \bar{C}_{2i})$ is written

$$\begin{aligned} \bar{G}_{1i}(t) = & \sum_{w=1}^{\infty} \left[\left(P_2 \int_0^L \tilde{\xi}_{1i}(x) \frac{d\tilde{\xi}_{1w}(x)}{dx} dx \right) \bar{C}_{1w}(t) \right. \\ & \left. + \left(P_4 \int_0^L \tilde{\xi}_{1i}(x) \frac{d\tilde{\xi}_{2w}(x)}{dx} dx + P_5 \int_0^L \tilde{\xi}_{1i}(x) \tilde{\xi}_{2w}(x) dx \right) \bar{C}_{2w}(t) \right], \end{aligned} \quad (71a)$$

$$\begin{aligned} \bar{G}_{2i}(t) = & \sum_{w=1}^{\infty} \left[\left(Q_2 \int_0^L \tilde{\xi}_{2i}(x) \frac{d\tilde{\xi}_{2w}(x)}{dx} dx \right) \bar{C}_{2w}(t) \right. \\ & \left. + \left(Q_4 \int_0^L \tilde{\xi}_{2i}(x) \frac{d\tilde{\xi}_{1w}(x)}{dx} dx + Q_5 \int_0^L \tilde{\xi}_{2i}(x) \tilde{\xi}_{1w}(x) dx \right) \bar{C}_{1w}(t) \right]. \end{aligned} \quad (71b)$$

The transformed initial conditions are provided as follows:

$$\bar{C}_{1i}(0) = \int_0^L \tilde{\xi}_{1i}(x) \mathcal{N}(x|\mu_0, \sigma_0) dx, \quad (72)$$

$$\bar{C}_{2i}(0) = 0. \quad (73)$$

The coupled system of ordinary differential equations provided in Eq. (68) is solved using an implicit time integration scheme and the algorithm is implemented in Matlab. Once $\bar{C}_{ki}(t)$ is solved, $C_k(x, t)$ can be obtained by using the inverse formula (60). After the average concentration, i.e., zeroth-order solution is obtained, the two-dimensional solution can be reconstructed by superposition of the zeroth- and the higher-order solution, see Eqs. (53) and (54).

$$C_f(x, y, t) = C_1(x, t) + \frac{\epsilon \text{Pe}}{D_1} M(y) \frac{\partial C_1}{\partial x}, \quad (74)$$

$$C_m(x, y, t) = C_2(x, t) + \frac{\epsilon \text{Pe}}{D_2} N(y) \frac{\partial C_2}{\partial x} + C_\delta(x, y, t), \quad (75)$$

where C_δ is utilized to compensate the mismatch induced by neglecting higher-order solution. $C_\delta(x, y, t)$ is assumed to ensure the continuity condition at the interface $y = h_0$ and satisfy the boundary condition at $y = h^n$, i.e., $dC_\delta/dy \rightarrow 0$. One possible form is constructed as Eq. (76),

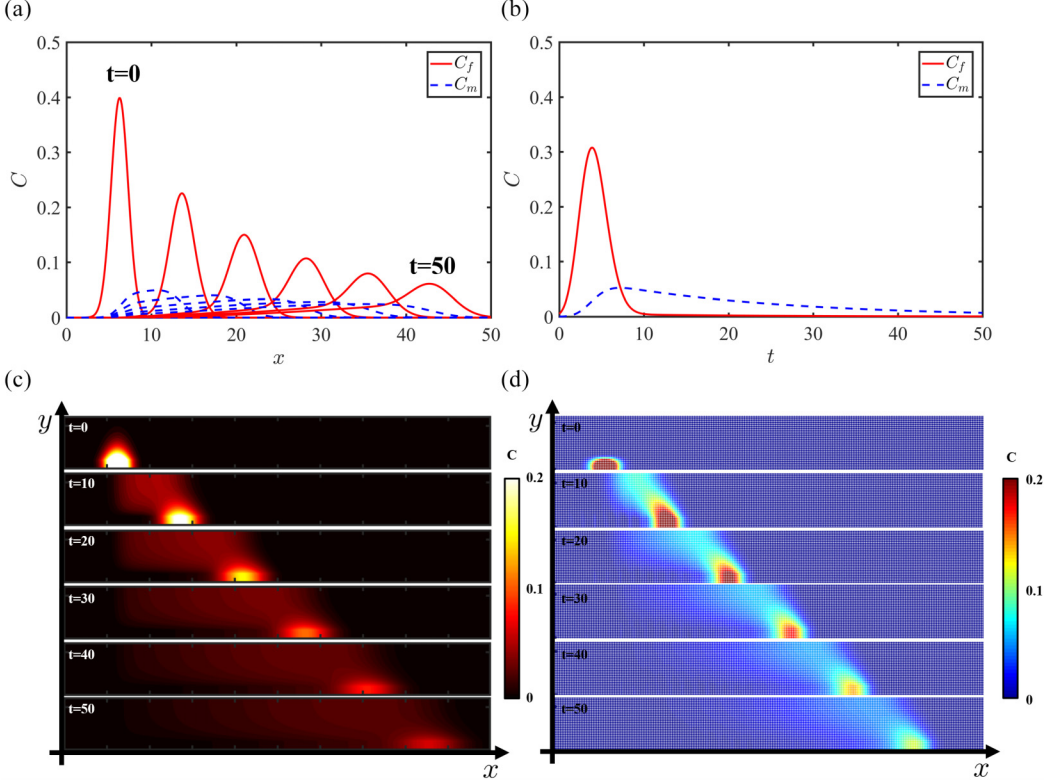


FIG. 3. (a) $C_1(x, t)$ and $C_2(x, t)$ spatial distribution at different times. (b) Concentration breakthrough curve (BTC) measured at $x = \mu_0 + 3\sigma_0$. (c) The reconstructed 2D solution of the concentration field using Eqs. (74) and (75). (d) The the concentration field of the 2D full solution.

which satisfies $C_f(x, h_0, t) = C_m(x, h_0, t)$ and decays to 0 as $y \rightarrow h^n$:

$$C_\delta(x, y, t) = [C_f(x, h_0, t) - C_m(x, h_0, t)]e^{h_0-y}. \quad (76)$$

In Fig. 3, we show the concentration field in a FFL- PML system. The length of the layer is $L = 50$, $h_0 = 1$, $[h_1, h_2, h_3] = [1, 3, 1]$, $[k_1, k_2, k_3] = [0.1, 0.01, 0.01]$, $D_1 = 1$, $D_2 = 1$, $Pe = 50$ and the total time computed is $T_{\text{final}} = 50$. Figure 3(a) shows the average concentration profile in the FFL (C_f) and in the PML (C_m) for $t = [0, 10, 20, 30, 40, 50]$. Figure 3(b) is the breakthrough curve (BTC) at $x = \mu_0 + 3\sigma_0$, where $\mu_0 = L/8$ and $\sigma_0 = 1$ are the mean and variance of the initial concentration distribution $\mathcal{N}(x|\mu_0, \sigma_0)$. Figure 3(c) illustrates the two-dimensional concentration reconstructed by Eqs. (74) and (75). We can see that the solute travels faster in the FFL and spreads wider in the PML [see Figs. 3(a) and 3(c)]. Such results indicate that the upscaled equation and the GITT algorithm provide a solution that is physically consistent. Figure 3(d) is the concentration field using the same setting solved by 2D full solver (see Sec. III B for solver details). As we can see, the reconstructed solution shows a high accuracy compared to the 2D full solution. The computation time of the upscaled equation is 36.06 s, while the 2D full solver takes 67.4 min.

B. Validation

To validate the one-dimensional upscaled equation and assess the accuracy of the solution, we compare the GITT solution with the results obtained from a two-dimensional partial differential equation solver. In our study, the two-dimensional case corresponds to the solution of Eqs. (34)

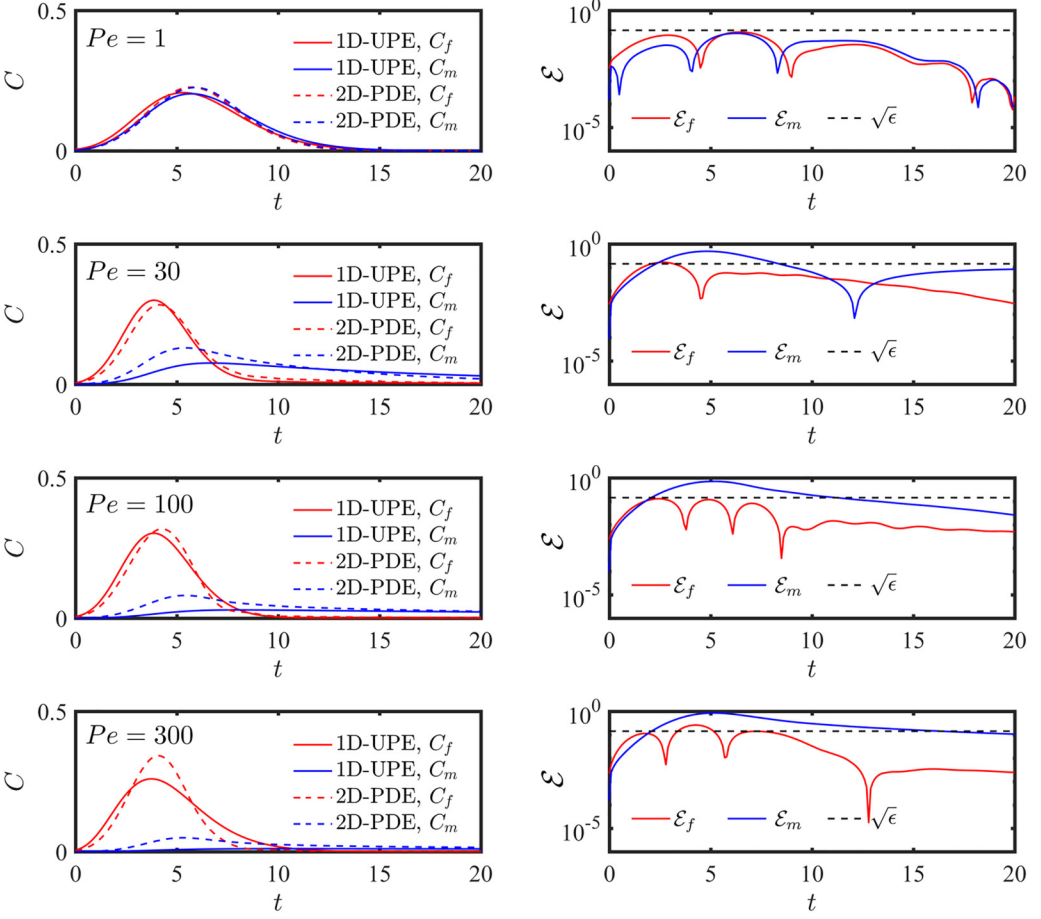


FIG. 4. Validation results of $Pe = 1$, $Pe = 30$, $Pe = 100$, and $Pe = 300$. The figures on the left are the BTCs measured at $x^* = \mu_0 + 3\sigma_0$ and the figures on the right are the error between the upscaled equation (1D-UPE) and two-dimensional result (2D-PDE). The black dashed line is the error threshold $\mathcal{E} = \sqrt{\epsilon}$.

and (35). The two-dimensional case, denoted here as 2D-PDE, is solved by the partial differential equation solver COMSOL Multiphysics, i.e., Coefficient-Form-PDE module. The upscaled equation is solved by GITT and is denoted as 1D-UPE. To assess the accuracy of the upscaled solution, we define the following error metric:

$$\mathcal{E}_{f,m}(t) = \frac{|C_{f,m}^{1D}|_{x=x^*} - C_{f,m}^{2D}|_{x=x^*}|}{\mathcal{N}(\mu_0|\mu_0, \sigma_0)}, \quad (77)$$

where $C_{f,m}^{2D}|_{x=x^*}$ is the average concentration (along the y direction) of the two-dimensional solution. Here, $\mathcal{N}(\mu_0|\mu_0, \sigma_0)$ corresponds to the maximum concentration of the initial distribution, i.e., the Gaussian distribution evaluated at $x = \mu_0$. Here, we define $x^* = \mu_0 + 3\sigma_0$ as the location where the concentration BTC is measured.

Figure 4 shows the comparison between the GITT solution and the two-dimensional numerical results for different values of Pe . For the results depicted in Fig. 4, we used the following parameters values: $L = 50$, $h_0 = 1$, $[h_1, h_2, h_3] = [1, 3, 1]$, $[k_1, k_2, k_3] = [0.1, 0.01, 0.01]$, $D_1 = D_2 = 1$. As previously mentioned, the concentration BTCs are measured at $x^* = \mu_0 + 3\sigma_0$. All parameters are

kept the same for both 1D-UPE and 2D-PDE. The figures on the left-hand-side are BTCs and the ones on the right are the errors between the results of 1D-UPE and 2D-PDE [Eq. (77)]. Overall, 1D-UPE exhibits a good agreement with the 2D-PDE when $Pe < 1000$, and the FFL solution (C_f) behaves better when compared to the PML solution (C_m). The maximum error of C_f is less than $\sqrt{\epsilon}$: $\max(\mathcal{E}_f) < \sqrt{\epsilon}$, and the error of C_m exceeds $\sqrt{\epsilon}$: $\max(\mathcal{E}_m) > \sqrt{\epsilon}$ but converge to small values at large time. As previously mentioned, Appendix C also demonstrates how our computational results converge to the Taylor-Aris dispersion coefficient when the permeability approaches zero.

In this section, we have established a general workflow for solving the solute transport problem in FFL + PML system. We started with two-dimensional governing equations and obtained the upscaled equations which are coupled one-dimensional equations. The coupled upscaled equations are solved semianalytically using the GITT method.

IV. TRANSPORT PROCESS ANALYSIS

A. Breakthrough condition

Here we demonstrate the impact of a multilayered porous media system on transport of a passive scalar at different Pe numbers. The total length of the domain is $L = 50$, with the FFL thickness $h_0 = 1$. The thickness of the individual porous layers are given as $[h_1, h_2, h_3, h_4, h_5] = [1, 3, 5, 3, 1]$, and the corresponding permeabilities are specified by the following values $[k_1, k_2, k_3, k_4, k_5] = [0.01, 0.01, k_3, 0.01, 0.01]$. Here, k_3 represents the permeability of the third layer, which we consider for two different values: $k_3 = 0.01$ and $k_3 = 0.5$. The diffusion coefficients in the FFL and PML are denoted as $D_1 = 1$ and $D_2 = 1$. For the initial condition, we set the concentration at $t = 0$ as $C_1(t = 0) = \mathcal{N}(x|L/8, 1)$, and we measure the concentration BTC at the position $x = (7/8)L$, which is close to the outlet of the channel-matrix system.

Figure 5 illustrates the scalar concentration BTCs for six selected Pe values: $Pe = 1 \times 10^{-3}, 1 \times 10^{-2}, 1, 10, 100, 300$. The solid red curve corresponds to the concentration in the FFL for case where $k_3 = 0.01$, while the dashed red curve corresponds to the concentration in the FFL for $k_3 = 0.5$. Similarly, the blue solid line represents the concentration in the PML layer with $k_3 = 0.01$, and the blue dashed line represents $k_3 = 0.5$. Figure 5 reveals that when $Pe \ll 1$, specifically when $Pe = 1 \times 10^{-3}$, the concentrations (namely, C_f and C_m) are independent of the value of k_3 . This suggests that in the regime dominated by diffusion ($Pe \ll 1$), the variability of the permeability in the PML has minimal influence on the transport behavior. However, as the Péclet number increases, see cases for $Pe = 1 \times 10^{-2}$ and $Pe = 1$, the temporal dynamics of the scalar concentration obtained for different k_3 values begin to deviate from each other. This indicates that the variability of the permeability starts to play a significant role in transport. Note that in the Pe range of 1×10^{-3} to 1, the concentrations C_f and C_m overlap, and diffusion is the main transport mechanism. When Pe reaches 10, the variability of the permeability in the PML has a substantial impact on transport. This can be observed from the concentration BTC results, where C_f and C_m display different breakthrough conditions represented by the two dashed curves. Furthermore, the results for different k_3 values become distinguishable by comparing the dashed and solid lines. As the Péclet number is increased to 100 and 300, the concentration BTC results obtained for different k_3 values start to merge with each other. This interesting behavior can be attributed to the dominant advection transport effect, where the scalar cloud is transported swiftly due to the fluid flow in the FFL. In this case, the variability of the permeability of the porous system does not influence significantly the transport dynamics.

B. Local dispersion

To examine the effect of the PML's permeability variability on the solute transport, we analyze the dispersion of the scalar cloud within the system. Following Cirpka and Kitanidis [43], we

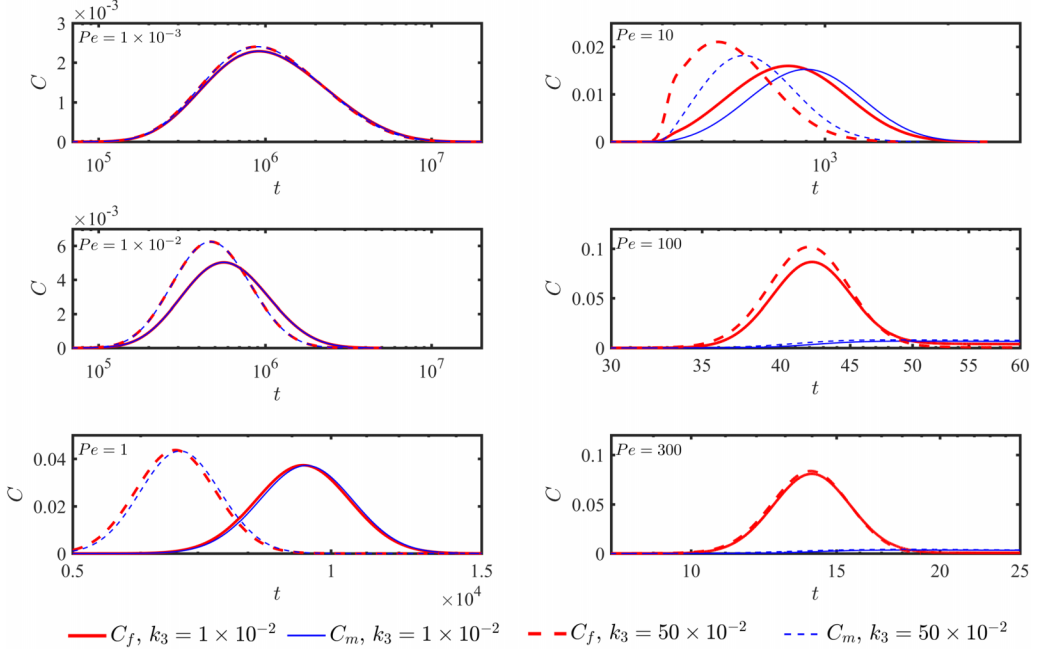


FIG. 5. Breakthrough curve (BTC) of an FFL + PML (five layers) system at different Pe numbers. The solid line represents a case of lower permeability, while the dashed line represents higher permeability results. The red curves depict the BTC of the FFL, and the blue curves correspond to the PML. In the low Pe case, all curves overlap, indicating similar transport processes. However, as $Pe \sim 10$, the curves diverge significantly, indicating a strong impact of the geometry.

compute the local temporal moments of the concentration BTCs:

$$\chi_{0,\gamma} = \int C_\gamma(x_0, t) dt, \quad (78)$$

$$\chi_{1,\gamma} = \int C_\gamma(x_0, t) t dt, \quad (79)$$

$$\chi_{2,\gamma} = \int C_\gamma(x_0, t) t^2 dt, \quad \text{for } \gamma = \{m, f\}, \quad (80)$$

where $C_\gamma(x_0, t)$ is the BTC of FFL ($\gamma = f$) or PML ($\gamma = m$) at $x = x_0$ and χ_i is the i^{th} temporal moment. The second central moment is defined by

$$\chi_{c,\gamma} = \chi_{2,\gamma} - \frac{\chi_{1,\gamma}^2}{\chi_{0,\gamma}}. \quad (81)$$

Therefore, the local dispersion can be computed as [43]

$$D_{\text{loc},\gamma} = \frac{x_{0,\gamma}^2 \chi_{c,\gamma} \chi_{0,\gamma}^2}{2\chi_{1,\gamma}^3}. \quad (82)$$

For the purpose of illustration, we investigate the influence of permeability on local dispersion within a three-layer system. The domain has a total length of $L = 40$, with the thickness of the FFL being $h_0 = 1$. The individual porous layer thicknesses are given as $[h_1, h_2, h_3] = [1, 5, 1]$, and the corresponding permeabilities are specified by $[k_1, k_2, k_3] = [0.01, k_2, 0.01]$, with k_2 taking values of 0.01 or 0.5. The local BTC used for dispersion computation is measured at position $x = 7L/8$,

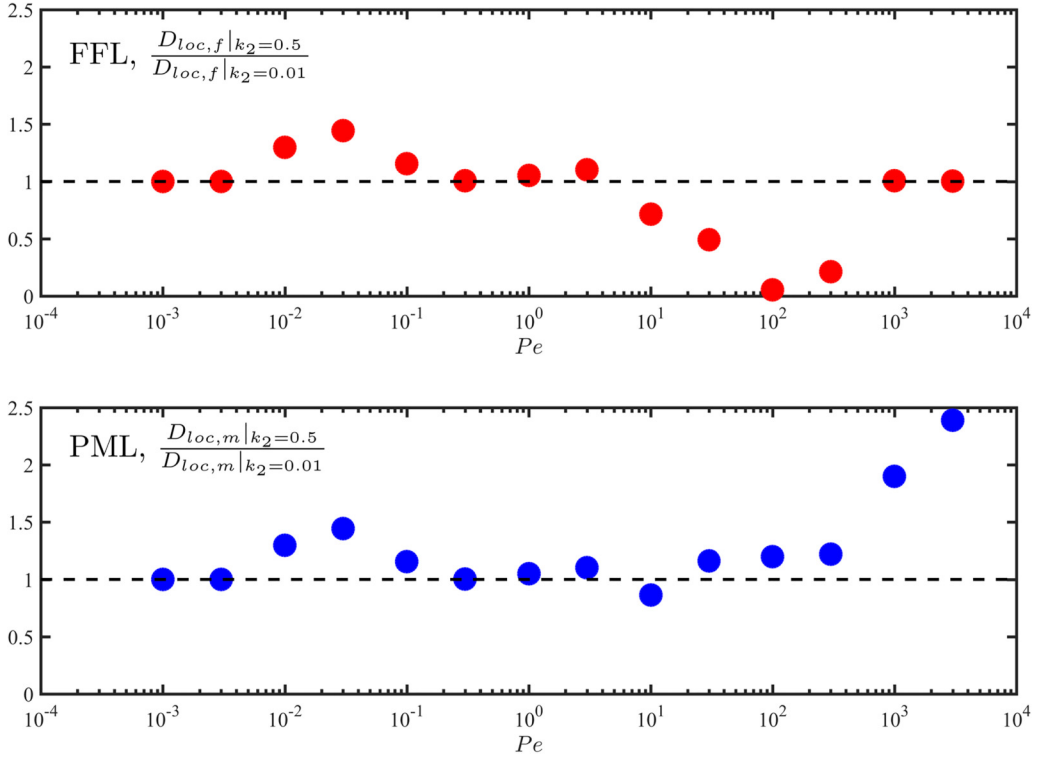


FIG. 6. The dispersion coefficient ratio is computed between different permeability cases. Each dot's value is determined by dividing the dispersion of the high permeability case by that of the low permeability case. The dashed line represents a ratio of 1; dots above the dashed line indicate that the dispersion of the high permeability case is larger.

which is equal to 35.0. We use $D_{loc,f}$ to denote the dispersion measured in the FFL and $D_{loc,m}$ for the dispersion measured in the PML.

Figure 6 presents the ratio of the local dispersion in the high permeability case ($D_{loc}|_{k_2=0.5}$) to that in the low permeability case ($D_{loc}|_{k_2=0.01}$). The top figure displays the ratio for the FFL, while the bottom figure represents the results for the PML. The Péclet number ranges from 1×10^{-3} to 3×10^3 . We plot the ratio to determine which configuration yields a higher local dispersion. Specifically, when the dot lies above the dashed line $D_{loc}|_{k_2=0.5} > D_{loc}|_{k_2=0.01}$, it signifies that the high permeability configuration results in a greater local dispersion.

In the FFL, when $Pe \ll 1$, the system is diffusion governed, and as a result, the dispersion coefficients are similar. For $Pe \in [1 \times 10^{-2}, 1 \times 10^{-1}]$, the high permeability configuration provides a higher local dispersion. Conversely, when $Pe \in [1 \times 10^1, 1 \times 10^3]$, the low permeability case leads to a higher FFL dispersion. When $Pe > 1 \times 10^3$, the system is dominated by advection, causing the BTCs to be similar due to the high flow rate that rapidly transports the scalar cloud. This is further confirmed in Fig. 5.

In the PML layer, dispersion escalates alongside the enhanced permeability of the third layer. As the permeability of a layer increases, velocity heterogeneity intensifies, leading to elevated dispersion.

In this section, we demonstrate how the upscaled system is solved by GITT, and the validation of the solution. Additionally, we analyze the BTCs in both FFL and PML together with computed local dispersion value. The results suggest that, permeability of the multilayers system has a strong impact on the system scale solute transport process.

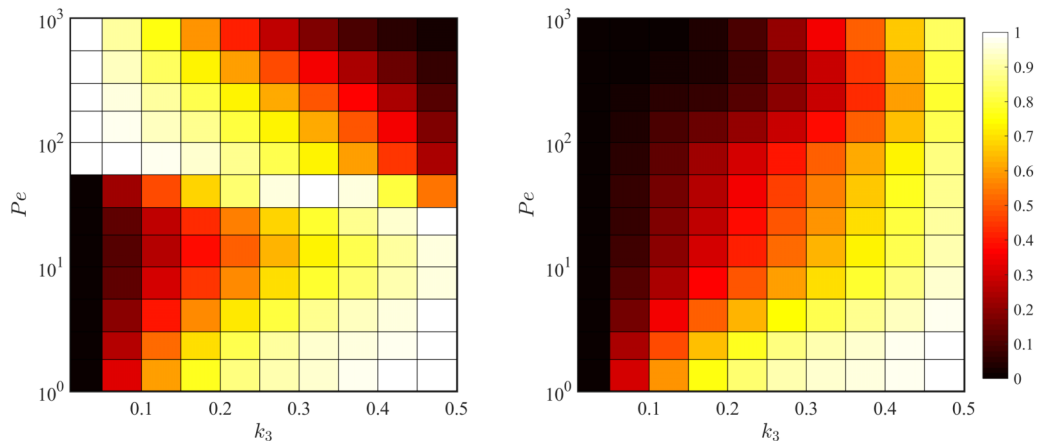


FIG. 7. The normalized dispersion computed based on the simulation results, see Eq. (83) of a FFL-PML (five layers) system for different Pe numbers and k_3 values. Each pixel is the result of a pair of k_3 -Pe, when the color is warmer/brighter, the dispersion is larger.

V. DISPERSION OPTIMIZATION

In the previous section, we demonstrated how permeability of one layer of the multilayered system changes the overall dispersion of the solute transport. These results showed the existence of a set of parameters that can potentially lead to an optimal dispersion. For example, can we identify a maximum dispersion at a given operating condition (i.e., Pe)? Such optimization is relevant for designing multilayered and evaluating solute mass transfer when the conductive properties of a certain layer changes.

To demonstrate this, we performed computations in a system with $L = 40$ and $h_0 = 1$. The thickness of the individual layers are given as $[h_1, h_2, h_3, h_4, h_5] = [1, 3, 5, 3, 1]$, and the corresponding permeabilities are specified by $[k_1, k_2, k_3, k_4, k_5] = [0.01, 0.01, k_3, 0.01, 0.01]$. Here, k_3 represents the permeability of the third layer. For this third layer, we consider six different permeability values: $k_3 = 0.01, 0.1, 0.2, 0.3, 0.4, 0.5$. The Pe number ranges from 1 to 1×10^3 , and the local dispersion computed at different k_3 is normalized using the following expression:

$$D_n = \frac{D_{\text{loc}}(\text{Pe})|_{k_3} - \min [D_{\text{loc}}(\text{Pe})|_{k_3}]}{\max [D_{\text{loc}}(\text{Pe})|_{k_3}] - \min [D_{\text{loc}}(\text{Pe})|_{k_3}]}, \quad (83)$$

for $k_3 = [0.01, 0.1, 0.2, 0.3, 0.4, 0.5]$.

Figure 7 depicts the results of the dispersion optimization. Figure 7 (left) provides the results of the FFL dispersion while the Fig. 7 (right) corresponds to the results of PML. Similar to the results shown in the dispersion analysis (Fig. 6), when Pe is small, highly permeable system provides a higher FFL dispersion which may enhance the mixing in the free-flow zone. When Pe is high, the permeable layer does not increase the dispersion in the free-flow zone. However, in the PML, a highly permeable third layer (i.e., $k_3 = 0.5$) always provides a higher dispersion.

With the same setup, we explore the design space by varying the third layer's thickness $h = [1, 3, h_3, 3, 1]$ and permeability $k = [0.01, 0.01, k_3, 0.01, 0.01]$. For each pair of h_3 and k_3 , we compute the dispersion coefficient $D_{\text{loc}}(\text{Pe})|_{h_3, k_3}$ using Eq. (82), and the normalized dispersion is

$$D_n = \frac{D_{\text{loc}}(\text{Pe})|_{h_3, k_3} - \min [D_{\text{loc}}(\text{Pe})|_{h_3, k_3}]}{\max [D_{\text{loc}}(\text{Pe})|_{h_3, k_3}] - \min [D_{\text{loc}}(\text{Pe})|_{h_3, k_3}]}, \quad (84)$$

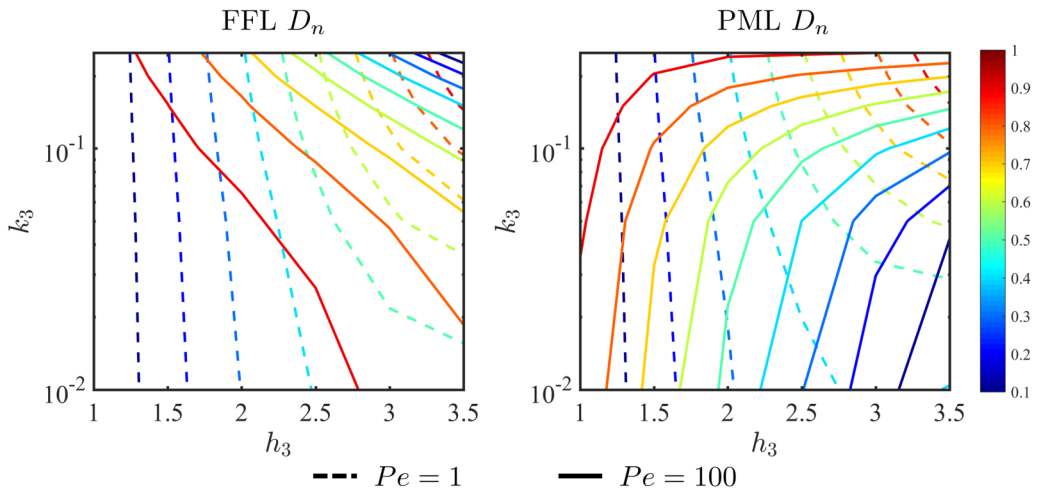


FIG. 8. Contour plots of the normalized dispersion as a function of k_3 and h_3 . Each line represents dispersion of the same value. The solid line is the higher Pe case and the dashed line denotes the lower Pe results.

where

$$h_3 = [1, 1.5, 2, 2.5, 3, 3.5], \quad (85)$$

$$k_3 = [0.01, 0.1, 0.2, 0.3, 0.4, 0.5]. \quad (86)$$

As shown in Fig. 8, the results for $Pe = 1$ (dashed lines) and $Pe = 100$ (solid lines) are displayed, with warm colors indicating high dispersion. When Pe is small, the maximum dispersion in the FFL occurs in a zone with large values of k_3 and h_3 . However, for $Pe = 100$, the maximum dispersion in the FFL can be achieved with small values of k_3 and h_3 . In the highly advective transport regime ($Pe = 100$), a wider porous media layer stretches the velocity profile and reduces the velocity heterogeneity along the y direction, leading to a weakening of the dispersive effects.

When h_3 is fixed at $Pe = 100$, a larger value of k_3 allows more flow to pass through the PML instead of the FFL, resulting in a decrease in the dispersivity (D_n). However, as shown in the right plot of Fig. 8, dispersion always increases as the permeability in the third layer increases. Furthermore, Fig. 8 indicates that it is possible to achieve the same dispersion coefficient with different combinations of k_3 and h_3 . This expands the parameter space for designing multilayer structures, such as microfluidics or membranes, to meet specific scalar transport requirements.

VI. SUMMARY

In this work, we analyze scalar transport in a two-dimensional shear-flow system consisting of a conduit bounded by a layered porous medium. Flow in the conduit is governed by Stokes equation, while flow in the porous medium is given by the Darcy-Brinkman equation. Transport of a passive scalar is computed through an upscaled one-dimensional model. The upscaled advection-dispersion equation is attained through the use of perturbation theory and spatial averaging. The upscaled concentration field is computed through the use of a hybrid analytical-numerical integral transforms method known as the generalized integral transform technique [39]. The Darcy-Brinkman flow model is used for the sake of illustration and the integral transform-based methodology employed for the scalar transport problem in this work is flexible to incorporate different flow models in the porous medium. We point out that other hybrid numerical-analytical approaches could be used to solve the upscaled advection-dispersion equations, such as the method proposed in de Barros *et al.* [44]. The integral transform approach proposed in de Barros *et al.* [44] yields a semianalytical solution. It

combines complex analysis with numerics and avoids the solution of ordinary differential equations. It is particularly well-suited to tackle partial differential equations with constant coefficients, such as 1D upscaled equations derived in this work. However, the GITT is a flexible method that allows to solve governing equations that exhibit coefficients that vary in both space and time [20,39]. The two-dimensional solution is reconstructed with the upscaled equation results. We successfully compare the results from the upscaled one-dimensional advection-dispersion equation with fully numerical results for the corresponding two-dimensional system.

Our research findings highlight the substantial influence of variations in the permeability field within a multilayered porous medium on the overall behavior of scalar mixing. We observed that the distribution of permeability within the porous medium significantly affects the dispersion of the scalar substance. Specifically, we identified the existence of an optimal dispersion coefficient that corresponds to the most efficient mixing in this type of system. The discovery of an optimal dispersion coefficient has important implications for engineering design. It suggests that by appropriately adjusting the permeability field, engineers can achieve an ideal level of dispersion that maximizes mixing efficiency. This knowledge can be applied to various engineering applications where effective mixing is crucial, such as in chemical reactors or environmental remediation processes. Furthermore, our study demonstrated that different combinations of properties within the porous media layer can lead to the same dispersion coefficient. This indicates that there is flexibility in designing porous media systems for efficient mixing. Engineers can explore various combinations of permeability, porosity, and other properties to achieve the desired dispersion coefficient, providing greater control over the mixing process.

Although outside of the scope of this work, it is important to note that in natural porous media, properties such as the permeability are uncertain due to data scarcity (e.g., Ref. [45]). Therefore transport quantities, such as the scalar concentration, must be characterized statistically. Under these conditions, the proposed integral transform solutions can be used in existing uncertainty analysis frameworks and modular computational packages, see Olivier *et al.* [46]. Furthermore, the results regarding solute mixing and dispersion are limited to the physical setup presented in this study. However, as previously mentioned, the computational approach proposed illustrates how the distribution of the permeabilities values can significantly impact the solute mixing rates. As shown in the results, the combination of the upscaled system and the integral transform method can be utilized to optimize solute dispersion and mixing.

Overall, these findings expand the possibilities for designing efficient mixing systems in engineering applications. By understanding the impact of permeability field variability and the existence of an optimal dispersion coefficient, engineers can optimize the design of porous media systems to enhance mixing and improve overall system performance.

ACKNOWLEDGMENTS

B.L. gratefully acknowledges partial support by the National Natural Science Foundation of China (NSFC), through the Award No. 42272158. F.P.J.d.B. acknowledges the partial support from NSF Award No. 1654009. All authors acknowledge the constructive comments raised by the reviewers and the editor.

The authors report no conflict of interest

APPENDIX A: ASYMPTOTIC EXPANSION

Substituting Eqs. (42), (43), and (44) into Eqs. (34) and (35) leads to

$$\begin{aligned} & \epsilon \text{Pe} \left(\frac{\partial c_1^{(0)}}{\partial t} + \epsilon^{\frac{1}{2}} \frac{\partial c_1^{(1)}}{\partial t} + \epsilon \frac{\partial c_1^{(2)}}{\partial t} \right) + \epsilon^{\frac{1}{2}} \text{Pe} \left(u_f \frac{\partial c_1^{(0)}}{\partial \eta} + \epsilon^{\frac{1}{2}} u_f \frac{\partial c_1^{(1)}}{\partial \eta} + \epsilon u_f \frac{\partial c_1^{(2)}}{\partial \eta} \right) \\ & = \epsilon D_1 \left(\frac{\partial^2 c_1^{(0)}}{\partial \eta^2} + \epsilon^{\frac{1}{2}} \frac{\partial^2 c_1^{(1)}}{\partial \eta^2} + \epsilon \frac{\partial^2 c_1^{(2)}}{\partial \eta^2} \right) + D_f \left(\epsilon^{\frac{1}{2}} \frac{\partial^2 c_1^{(1)}}{\partial y^2} + \epsilon \frac{\partial^2 c_1^{(2)}}{\partial y^2} \right) \end{aligned} \quad (\text{A1})$$

and

$$\begin{aligned} & \epsilon \text{Pe} \left(\frac{\partial c_2^{(0)}}{\partial t} + \epsilon^{\frac{1}{2}} \frac{\partial c_2^{(1)}}{\partial t} + \epsilon \frac{\partial c_2^{(2)}}{\partial t} \right) + \epsilon^{\frac{1}{2}} \text{Pe} \left(u_m \frac{\partial c_2^{(0)}}{\partial \eta} + \epsilon^{\frac{1}{2}} u_m \frac{\partial c_2^{(1)}}{\partial \eta} + \epsilon u_m \frac{\partial c_2^{(2)}}{\partial \eta} \right) \\ & = \epsilon D_2 \left(\frac{\partial^2 c_2^{(0)}}{\partial \eta^2} + \epsilon^{\frac{1}{2}} \frac{\partial^2 c_2^{(1)}}{\partial \eta^2} + \epsilon \frac{\partial^2 c_2^{(2)}}{\partial \eta^2} \right) + D_m \left(\epsilon^{\frac{1}{2}} \frac{\partial^2 c_2^{(1)}}{\partial y^2} + \epsilon \frac{\partial^2 c_2^{(2)}}{\partial y^2} \right), \end{aligned} \quad (\text{A2})$$

respectively. Collecting terms that have the same order of magnitude of ϵ :

$$\text{Pe} u_f \frac{\partial c_1^{(0)}}{\partial \eta} = D_1 \frac{\partial^2 c_1^{(1)}}{\partial y^2}, \quad (\text{A3})$$

$$\text{Pe} \frac{\partial c_1^{(0)}}{\partial t} + \text{Pe} u_f \frac{\partial c_1^{(1)}}{\partial \eta} = D_1 \frac{\partial^2 c_1^{(0)}}{\partial \eta^2} + D_1 \frac{\partial^2 c_1^{(2)}}{\partial y^2}, \quad (\text{A4})$$

$$\text{Pe} \frac{\partial c_1^{(1)}}{\partial t} + \text{Pe} u_f \frac{\partial c_1^{(2)}}{\partial \eta} = D_1 \frac{\partial^2 c_1^{(1)}}{\partial \eta^2}, \quad (\text{A5})$$

and for the porous domain:

$$\text{Pe} u_m \frac{\partial c_2^{(0)}}{\partial \eta} = D_2 \frac{\partial^2 c_2^{(1)}}{\partial y^2}, \quad (\text{A6})$$

$$\text{Pe} \frac{\partial c_2^{(0)}}{\partial t} + \text{Pe} u_m \frac{\partial c_2^{(1)}}{\partial \eta} = D_2 \frac{\partial^2 c_2^{(0)}}{\partial \eta^2} + D_2 \frac{\partial^2 c_2^{(2)}}{\partial y^2}, \quad (\text{A7})$$

$$\text{Pe} \frac{\partial c_2^{(1)}}{\partial t} + \text{Pe} u_m \frac{\partial c_2^{(2)}}{\partial \eta} = D_2 \frac{\partial^2 c_2^{(1)}}{\partial \eta^2}, \quad (\text{A8})$$

The corresponding conditions are

$$\langle c_1^{(1)} \rangle = 0, \quad (\text{A9})$$

$$\langle c_1^{(2)} \rangle = 0, \quad (\text{A10})$$

$$\frac{\partial c_1^{(1)}}{\partial y} = 0, \quad y = 0, \quad (\text{A11})$$

$$\frac{\partial c_1^{(2)}}{\partial y} = 0, \quad y = 0, \quad (\text{A12})$$

$$\langle c_2^{(1)} \rangle = 0, \quad (\text{A13})$$

$$\langle c_2^{(2)} \rangle = 0, \quad (\text{A14})$$

$$\frac{\partial c_2^{(1)}}{\partial y} = 0, \quad y = 0, \quad (\text{A15})$$

$$\frac{\partial c_2^{(2)}}{\partial y} = 0, \quad y = 0, \quad (\text{A16})$$

$$c_1^{(0)} + \epsilon^{\frac{1}{2}} c_1^{(1)} + \epsilon c_1^{(2)} = c_2^{(0)} + \epsilon^{\frac{1}{2}} c_2^{(1)} + \epsilon c_2^{(2)}, \quad (\text{A17})$$

$$D_1 \frac{\partial c_1^{(1)}}{\partial y} = \phi D_2 \frac{\partial c_2^{(1)}}{\partial y}, \quad y = 1, \quad (\text{A18})$$

$$D_1 \frac{\partial c_1^{(2)}}{\partial y} = \phi D_2 \frac{\partial c_2^{(2)}}{\partial y}, \quad y = 1. \quad (\text{A19})$$

Integration of Eq. (A3) together with conditions (A9) and (A11) gives

$$c_1^{(1)} = \frac{\epsilon^{\frac{1}{2}} \text{Pe}}{D_1} M(y) \frac{\partial c_1^{(0)}}{\partial x}, \quad (\text{A20})$$

where $M(y)$ is given by Eq. (B1). Similarly, integration of Eq. (A6) gives

$$c_2^{(1)} = \frac{\epsilon^{\frac{1}{2}} \text{Pe}}{D_2} N(y) \frac{\partial c_2^{(0)}}{\partial x}. \quad (\text{A21})$$

Procedure of getting the higher-order solution is shown in Ling *et al.* [13,3].

APPENDIX B: PARAMETERS

The parameters are

$$M(y) = I_{uf}(y) + F_1, \quad (\text{B1})$$

$$N(y) = I_{um}(y) + G_1 y + G_2, \quad (\text{B2})$$

$$A_1 = \phi N'(h_0), \quad (\text{B3})$$

$$A_2 = \frac{2\phi(h^n - h_0)D_m}{\epsilon \text{Pe}(1 + 2G_3 + 2G_4)}, \quad (\text{B4})$$

$$B_1 = \frac{N'(h_0)}{h^n - h_0}, \quad (\text{B5})$$

$$B_2 = \frac{2D_m}{\epsilon \text{Pe}(1 + 2G_3 + 2G_4)}, \quad (\text{B6})$$

where

$$I_{uf}(y) = \int \int_0^y u_f(y^*) dy^*, \quad (\text{B7})$$

$$I_{um}(y) = \int \int_{h_0}^y u_m(y^*) dy^*, \quad (\text{B8})$$

$$F_1 = -\langle I_{uf}(y) \rangle, \quad (\text{B9})$$

$$G_1 = -\int_{h_0}^{h^n} u_m(y) dy, \quad (\text{B10})$$

$$G_2 = -\langle I_{um}(y) \rangle - \langle G_1 y \rangle, \quad (\text{B11})$$

$$G_3 = -h^n, \quad (\text{B12})$$

$$G_4 = -\frac{(h^n)^3 + 3(h^n)^2 G_3 - 1 - 2G_3}{6h^n - 6}. \quad (\text{B13})$$

The variables of the Eqs. (55) and (56) are

$$P_1 = D_1^*, \quad P_2 = -\langle u_f \rangle, \quad P_3 = A_1, \quad P_4 = A_2, \quad P_5 = -A_2, \quad (\text{B14})$$

$$Q_2 = D_2^*, \quad Q_2 = -(\langle u_m \rangle + B_1), \quad Q_3 = 0, \quad Q_4 = B_2, \quad Q_5 = -B_2. \quad (\text{B15})$$

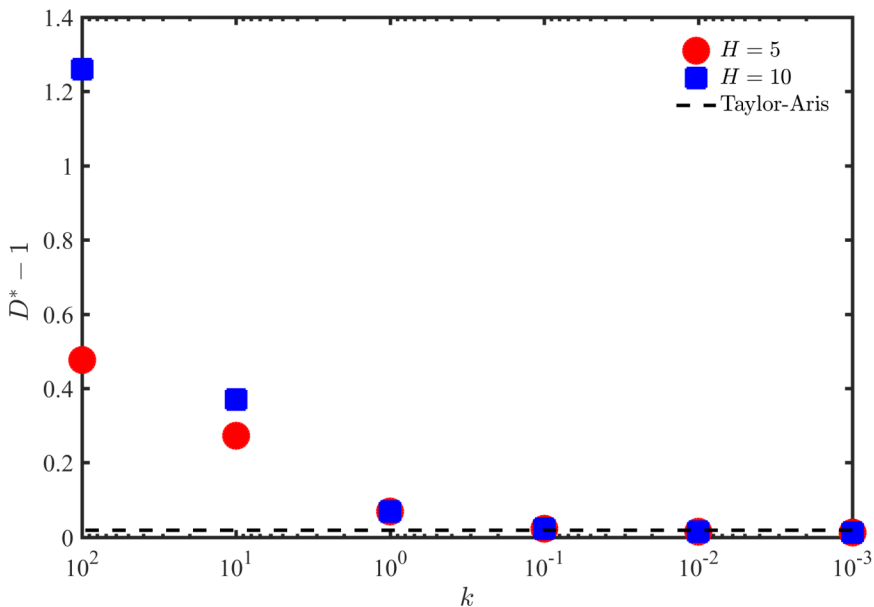


FIG. 9. Comparison between the classic Taylor-Aris dispersion (dashed line) and the upscaled dispersion of the FFL D_1^* .

APPENDIX C: VALIDATION WITH THE TAYLOR-ARIS DISPERSION THEORY

In this Appendix, we show how our computational results converge to the Taylor-Aris dispersion coefficient. D_1^* is the effective dispersion coefficient of the FFL. The classic Taylor-Aris dispersion coefficient of a slit is (see Eq. (72) of Dejam *et al.* [22])

$$D_{TA} = 1 + \frac{2}{105} \text{Pe}^2. \quad (\text{C1})$$

We expect D_1^* converges to D_{TA} when permeability approaches zero. To validate, we set single layer PML with $h = 5$ or $h = 10$ and compute D_1^* with $k = [1 \times 10^2, 1 \times 10^1, 1 \times 10^0, 1 \times 10^{-1}, 1 \times 10^{-2}, 1 \times 10^{-3}]$. We are using $\text{Pe} = 1$ and $\varepsilon = 1$ for the computation, since the prefactor is not a function of Pe and ε . The result is shown in Fig. 9. We plot $D_{TA} - 1$ using dashed line, and denote $D_1^* - 1$ using red dots ($H = 5$) and blue squares ($H = 10$). We can see that both solutions approaches to the Taylor-Aris when $k \rightarrow 0$.

-
- [1] E. A. Sudicky and E. O. Frind, Contaminant transport in fractured porous media: Analytical solutions for a system of parallel fractures, *Water Resour. Res.* **18**, 1634 (1982).
 - [2] M. Ghisalberti, Obstructed shear flows: Similarities across systems and scales, *J. Fluid Mech.* **641**, 51 (2009).
 - [3] B. Ling, A. M. Tartakovsky, and I. Battiato, Dispersion controlled by permeable surfaces: Surface properties and scaling, *J. Fluid Mech.* **801**, 13 (2016).
 - [4] S. Weinbaum, X. Zhang, Y. Han, H. Vink, and S. C. Cowin, Mechanotransduction and flow across the endothelial glycocalyx, *Proc. Natl. Acad. Sci. USA* **100**, 7988 (2003).
 - [5] M. Al-Chidiac, P. Mirbod, Y. Andreopoulos, and S. Weinbaum, Dynamic compaction of soft compressible porous materials: Experiments on air-solid phase interaction, *J. Porous Media* **12**, 1019 (2009).

- [6] P. Sanaei and L. J. Cummings, Flow and fouling in membrane filters: Effects of membrane morphology, *J. Fluid Mech.* **818**, 744 (2017).
- [7] D. Fong, L. J. Cummings, S. J. Chapman, and P. Sanaei, On the performance of multilayered membrane filters, *J. Eng. Math.* **127**, 23 (2021).
- [8] H. Deng, S. Molins, C. Steefel, J. Bargar, A. Jew, A. Hakala, C. Lopano, and W. Xiong, Modeling and experimental investigation of the evolution of altered zones at the shale-fluid interface, in *EGU General Assembly Conference Abstracts* (EGU, Munich, 2020), p. 21236.
- [9] Q. Li, A. D. Jew, A. Kohli, K. Maher, G. E. Brown Jr., and J. R. Bargar, Thicknesses of chemically altered zones in shale matrices resulting from interactions with hydraulic fracturing fluid, *Energy Fuels* **33**, 6878 (2019).
- [10] B. Ling, M. Sodwatana, A. Kohli, C. M. Ross, A. Jew, A. R. Kavscek, and I. Battiato, Probing multiscale dissolution dynamics in natural rocks through microfluidics and compositional analysis, *Proc. Natl. Acad. Sci. USA* **119**, e2122520119 (2022).
- [11] M. Dejam, Advective-diffusive-reactive solute transport due to non-Newtonian fluid flows in a fracture surrounded by a tight porous medium, *Int. J. Heat Mass Transf.* **128**, 1307 (2019).
- [12] M. Dejam, Hydrodynamic dispersion due to a variety of flow velocity profiles in a porous-walled microfluidic channel, *Int. J. Heat Mass Transf.* **136**, 87 (2019).
- [13] B. Ling, C. B. Rizzo, I. Battiato, and F. P. J. de Barros, Macroscale transport in channel-matrix systems via integral transforms, *Phys. Rev. Fluids* **6**, 044501 (2021).
- [14] M. Dejam and H. Hassanzadeh, Dispersion tensor in stratified porous media, *Phys. Rev. E* **105**, 065115 (2022).
- [15] J.-R. de Dreuzy, Y. Méheust, and G. Pichot, Influence of fracture scale heterogeneity on the flow properties of three-dimensional discrete fracture networks (DFN), *J. Geophys. Res.* **117**, (2012).
- [16] J. Erhel, J.-R. de Dreuzy, and B. Poirriez, Flow simulation in three-dimensional discrete fracture networks, *SIAM J. Sci. Comput.* **31**, 2688 (2009).
- [17] D. Roubinet, J.-R. de Dreuzy, and D. M. Tartakovsky, Semi-analytical solutions for solute transport and exchange in fractured porous media, *Water Resour. Res.* **48**, W01542 (2012).
- [18] D. Roubinet and D. M. Tartakovsky, Hybrid modeling of heterogeneous geochemical reactions in fractured porous media, *Water Resour. Res.* **49**, 7945 (2013).
- [19] D. Roubinet, J. Irving, and F. D. Day-Lewis, Development of a new semi-analytical model for cross-borehole flow experiments in fractured media, *Adv. Water Resour.* **76**, 97 (2015).
- [20] F. P. J. de Barros and R. M. Cotta, Integral transforms for three-dimensional steady turbulent dispersion in rivers and channels, *Appl. Math. Model.* **31**, 2719 (2007).
- [21] D. H. Tang, E. O. Frind, and E. A. Sudicky, Contaminant transport in fractured porous media: Analytical solution for a single fracture, *Water Resour. Res.* **17**, 555 (1981).
- [22] M. Dejam, H. Hassanzadeh, and Z. Chen, Shear dispersion in a fracture with porous walls, *Adv. Water Resour.* **74**, 14 (2014).
- [23] S. Rubol, I. Battiato, and F. P. J. de Barros, Vertical dispersion in vegetated shear flows, *Water Resour. Res.* **52**, 8066 (2016).
- [24] R. M. Cotta, K. M. Lisboa, and J. L. Z. Zotin, Integral transforms for flow and transport in discrete and continuum models of fractured heterogeneous porous media, *Adv. Water Resour.* **142**, 103621 (2020).
- [25] R. A. Zimmerman, G. Severino, and D. M. Tartakovsky, Hydrodynamic dispersion in a tube with diffusive losses through its walls, *J. Fluid Mech.* **837**, 546 (2018).
- [26] U. Hornung, *Homogenization and Porous Media* (Springer, New York, NY, 1997).
- [27] S. Whitaker, *The Method of Volume Averaging* (Kluwer Academic Publishers, Netherlands, 1999), pp. 1–70.
- [28] H. Brenner, *Transport Processes in Porous Media* (McGraw-Hill, New York, NY, 1987).
- [29] G. Matheron and G. De Marsily, Is transport in porous media always diffusive? A counterexample, *Water Resour. Res.* **16**, 901 (1980).
- [30] A. Fiori and G. Dagan, Transport of a passive scalar in a stratified porous medium, *Transport Porous Med.* **47**, 81 (2002).

- [31] M. Barroso, N. Touze-Foltz, K. von Maubeuge, and P. Pierson, Laboratory investigation of flow rate through composite liners consisting of a geomembrane, a GCL, and a soil liner, *Geotext. Geomembranes* **24**, 139 (2006).
- [32] M. Dentz and F. P. J. de Barros, Mixing-scale dependent dispersion for transport in heterogeneous flows, *J. Fluid Mech.* **777**, 178 (2015).
- [33] M. Dentz, T. Le Borgne, and J. Carrera, Effective transport in random shear flows, *Phys. Rev. E* **77**, 020101(R) (2008).
- [34] D. Bolster, F. J. Valdés-Parada, T. LeBorgne, M. Dentz, and J. Carrera, Mixing in confined stratified aquifers, *J. Contam. Hydrol.* **120-121**, 198 (2011).
- [35] N. Wang, Y. Si, N. Wang, G. Sun, M. El-Newehy, S. S. Al-Deyab, and B. Ding, Multilevel structured polyacrylonitrile/silica nanofibrous membranes for high-performance air filtration, *Sep. Purif. Technol.* **126**, 44 (2014).
- [36] S. C. Hirata, B. Goyeau, and D. Gobin, Stability of natural convection in superposed fluid and porous layers: Influence of the interfacial jump boundary condition, *Phys. Fluids* **19**, 058102 (2007).
- [37] S. C. Hirata, B. Goyeau, D. Gobin, M. Carr, and R. M. Cotta, Linear stability of natural convection in superposed fluid and porous layers: Influence of the interfacial modelling, *Int. J. Heat Mass Transf.* **50**, 1356 (2007).
- [38] G. S. Beavers and D. D. Joseph, Boundary conditions at a naturally permeable wall, *J. Fluid Mech.* **30**, 197 (1967).
- [39] R. M. Cotta, *Integral Transforms in Computational Heat and Fluid Flow* (CRC Press, Boca Raton, FL, 1993).
- [40] R. M. Cotta, D. C. Knupp, C. P. Naveira-Cotta, L. A. Sphaier, and J. N. N. Quaresma, Unified integral transforms algorithm for solving multidimensional nonlinear convection-diffusion problems, *Numer. Heat Transfer, Part A* **63**, 840 (2013).
- [41] F. P. J. de Barros, W. B. Mills, and R. M. Cotta, Integral transform solution of a two-dimensional model for contaminant dispersion in rivers and channels with spatially variable coefficients, *Environ. Modell. Software* **21**, 699 (2006).
- [42] M. D. Mikhailov and M. N. Ozisik, *Unified Analysis and Solutions of Heat and Mass Diffusion* (Dover Publications, Mineola, NY, 1994).
- [43] O. A. Cirpka and P. K. Kitanidis, Characterization of mixing and dilution in heterogeneous aquifers by means of local temporal moments, *Water Resour. Res.* **36**, 1221 (2000).
- [44] F. P. J. de Barros, M. J. Colbrook, and A. S. Fokas, A hybrid analytical-numerical method for solving advection-dispersion problems on a half-line, *Int. J. Heat Mass Transf.* **139**, 482 (2019).
- [45] G. Dagan, Solute transport in heterogeneous porous formations, *J. Fluid Mech.* **145**, 151 (1984).
- [46] A. Olivier, D. G. Giovanis, B. S. Aakash, M. Chauhan, L. Vandanapu, and M. D. Shields, UQpy: A general purpose Python package and development environment for uncertainty quantification, *J. Comput. Sci.* **47**, 101204 (2020).